Quantum magnets with weakly confined spinons: Multiple length scales and quantum impurities

R. L. Doretto and Matthias Vojta
Institut für Theoretische Physik, Universität zu Köln, Zülpicher Straße 77, 50937 Köln, Germany
(Received 7 April 2009; published 10 July 2009)

In magnets with strong quantum fluctuations, paramagnetic ground states with or without confinement of spinon excitations can be realized. Here we discuss the physics of the confined phase in the vicinity of a confinement-deconfinement transition: this regime, likely relevant to a multitude of frustrated spin systems, is characterized by multiple length scales. In addition to the magnetic correlation length, a confinement length can be defined, which can be probed, e.g., by local static measurements near nonmagnetic impurities. We illustrate the ideas by explicit calculations for dimerized spin chains, but our qualitative results remain valid in higher dimensions as well. In particular, we study crossover from weak to strong confinement visible in the antiferromagnetic polarization cloud around a nonmagnetic impurity. We also discuss the effective magnetic interaction between impurities, relevant for impurity-induced magnetic order, and consequences for nuclear magnetic resonance and neutron-scattering experiments.

DOI: 10.1103/PhysRevB.80.024411 PACS number(s): 75.10.Jm, 75.40.Mg, 75.50.Ee

I. INTRODUCTION

The last decades have seen tremendous interest in exotic phases of correlated quantum matter characterized by elementary excitations with fractional quantum numbers. Some examples are Luttinger liquids,[1] spin liquids,[2] and fractional quantum Hall systems.[3] While it has long been known that fractionalization generically occurs in one space dimension (1D), the situation in higher dimensions D is quite different. It has become clear that fractionalized phases in $D \geq 2$ can be connected to deconfined phases of certain lattice gauge theories.[4,5]

Quantum antiferromagnets have played a central role in investigations of exotic phases.[5] Such systems can exhibit both antiferromagnetic and paramagnetic ground states. In the latter situation, which is generic to 1D due to the Mermin-Wagner theorem, quantum fluctuations prevent long-range order of the spins. In $D \geq 2$, quantum paramagnetic states may obtained by the formation of singlet bonds of spins 1/2. For lattices with one spin 1/2 per unit cell, the singlet bonds can form either crystalline order accompanied by lattice symmetry breaking, leading to so-called valence bond solid (VBS) phases, or short-range ordered liquid states without any broken symmetry.[5] Remarkably, such spin liquids can be shown to be fractionalized, with elementary excitations being spin-1/2 spinons.

The search for microscopic realizations of spin liquids in $D \geq 2$ remains difficult because the relevant spin models display geometric frustration: this reduces the applicability of otherwise powerful quantum Monte Carlo techniques due to the so-called sign problem. The first unambiguous demonstration of a stable phase with fractionalization in two-dimensional (2D) magnet was for the triangular-lattice quantum dimer model, which features both VBS and gapped spin-liquid phases, the latter displaying topological order.[6] Models with exact gapped spin-liquid ground states have been constructed, such as the toric code model[7] and the spin-1/2 honeycomb model,[8] both due to Kitaev. Heisenberg models with longer-range frustrated interactions are believed to be good candidates for topological spin liquids as well, but with the exception of the triangular-lattice ring-exchange model[9] no conclusive numerical results are available. (Gapless spin liquids with power-law correlation functions do not play a role in the subsequent discussion.)

A special form of fractionalization has been argued to be possible at a continuous quantum phase transition between two conventional phases with different broken symmetries.[10] A candidate for this scenario of deconfined quantum criticality is the Néel-VBS transition of the square-lattice Heisenberg antiferromagnet supplemented by a ring-exchange interaction.[11] An interesting prediction of the deconfined critical theory is the existence of two distinct small energy scales on the VBS side of the quantum critical point: primarily, the transition is between a Néel state and a spin liquid and the VBS is a secondary instability of the spin liquid. Consequently, dimerization and confinement set in at a much smaller energy scale compared to paramagnetic behavior.

A common feature of (i) a confined paramagnet near a confinement-deconfinement transition and (ii) a VBS phase near a deconfined critical point is that, in addition to the magnetic correlation length ξ_{mag}, there exists a much larger length scale associated with confinement, which we dub confinement length ξ_{conf}. In the following, we shall understand ξ_{conf} as the typical spatial extension of a two-spinon bound state. Importantly, both ξ_{conf} and ξ_{mag} can be large compared to microscopic lengths, opening the possibility to find universal phenomena characterized by two length scales, in contrast to the conventional situation with ξ_{mag} being the only large length. Indeed, a recent numerical study[12] of the frustrated regime of the $J_1-J_2-J_3$ Heisenberg antiferromagnet on a square lattice gave evidence for two distinct length scales, with $\xi_{\mathrm{conf}} > \xi_{\mathrm{mag}}$.

The purpose of this paper is a detailed discussion of physical properties of quantum paramagnets near deconfinement. We believe this regime to be relevant for a rather broad class of frustrated magnets: even if the elementary excitations are ultimately confined, there will be signatures of deconfinement on shorter length scales, which can be probed experimentally. The presence of two length scales, ξ_{conf} and ξ_{mag}, strongly modifies a number of phenomena, both in statics and dynamics. We present general arguments and support

them by explicit calculations for 1D Heisenberg models. Although the mechanisms of fractionalization are quite different in 1D and higher dimensions, we argue that various consequences for observables are similar, and hence our results remain qualitatively valid in $D \geq 2$ as well.

A. Observables

In the simplest picture, weak confinement can be understood in terms of a (weak) linear potential, $V(x)=\alpha|x|$, describing the effective interaction between two spinons. The two-particle problem then has only bound-state solutions, i.e., all excitations are of two-spinon type. The lowest two-spinon triplet state takes the role of the conventional spin-1 (triplon) excitation, its size defining the confinement length ξ_{conf}, with $\xi_{\text{conf}} \to \infty$ for $\alpha \to 0$.

A static measurement of ξ_{conf} is possible, e.g., by spatial pinning of one of the two partners of the bound state. This can be achieved by doping with nonmagnetic impurities: removing one spin 1/2 from the system breaks a singlet and liberates a spinon, which now interacts with the vacancy (holon). Provided that the binding between spinon and holon is identical to that between two spinons, the size of the spinon-holon bound state gives a measure of ξ_{conf}. As we show below, the size of the antiferromagnetic polarization cloud around the vacancy is given by ξ_{conf} in the weakly confined regime (whereas it is determined by ξ_{mag} in the conventional case of strong confinement). This polarization cloud, which can be detected, e.g., by local magnetic probes, also determines the effective magnetic interaction between impurity moments and is hence relevant for impurity-induced magnetic order.

Weak confinement shows up as well in the dynamical properties, as it implies the existence of multiple bound states below the two- or three-triplon continuum. Hence, inelastic neutron-scattering experiments, measuring the dynamic spin susceptibility, will detect a series of sharp dispersing modes below the threshold of the multiparticle continuum.

With increasing confinement potential, ξ_{conf} decreases. The criterion for the crossover to strong confinement may be defined as $\xi_{\text{conf}} \sim \xi_{\text{mag}}$. This is expected to coincide with the condition that the energy spacing between the lowest two-spinon bound states becomes comparable to the spin gap, and hence the higher bound states are no longer discernible in the dynamical susceptibility.

B. Outline

The remainder of the paper is organized as follows. In Secs. II–V we discuss the physics of weak confinement in one dimension: Sec. II summarizes the well-known properties of the frustrated dimerized spin chain, described by the $J_1-J_2-\delta$ model, and the methods applied in the following sections. Numerical results for the undoped spin chain are discussed in Sec. III while analytical and numerical calculations for the system doped with a single vacancy are presented in Sec. IV. Section V describes experimental implications of weak confinement for nuclear magnetic resonance (NMR) and neutron-scattering measurements and for impurity-induced magnetic order. Finally, in Sec. VI we discuss the relevance of our findings for higher dimensions. A brief summary of our results closes the paper.

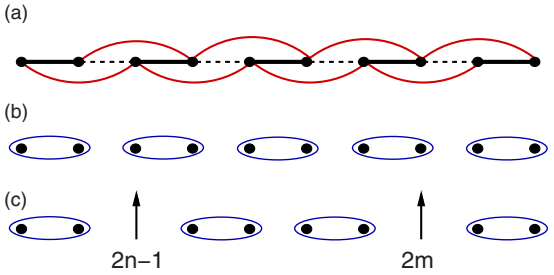

FIG. 1. (Color online) Schematic representations: (a) model Hamiltonian (1). The thick solid (black) lines correspond to a strong bond $[J_1(1+\delta)]$, the dashed lines to a weak bond $[J_1(1-\delta)]$, and the thin solid (red) lines to the J_2 coupling. (b) State $|0\rangle$. The ellipses represent singlet states between neighboring sites. (c) State $|nm\rangle$. The two spins at sites $2n-1$ and $2m$ are separated by a singlet pattern.

II. FRUSTRATED DIMERIZED SPIN CHAINS

In one space dimension, spinon excitations are quite generically deconfined. The standard spin-1/2 Heisenberg chain has a gapless excitation spectrum, while frustration can induce spontaneous dimerization leading to gapped (but still deconfined) spinons. To induce confinement, one has to resort to models with explicitly broken translational symmetry.

A. Model and phase diagram

We consider the so-called $J_1-J_2-\delta$ model, describing a frustrated dimerized antiferromagnetic (AF) spin chain:

$$H_{\text{ch}} = J_1 \sum_{i=1}^{2N} [1-(-1)^i \delta] \mathbf{S}_i \cdot \mathbf{S}_{i+1} + J_2 \sum_{i=1}^{2N} \mathbf{S}_i \cdot \mathbf{S}_{i+2}. \quad (1)$$

Here $\mathbf{S}_i$ represents a spin 1/2 at site i, J_1 and J_2 are the antiferromagnetic first- and second-neighbor exchange couplings, and δ denotes the degree of dimerization; see Fig. 1(a). (We will employ $J_1=1$ in the following.)

The ground-state phase diagram of model (1) in the $J_2-\delta$ plane is well known,[13,14] Fig. 2, and will be summarized in the following. We start with $\delta=0$. For small $J_2 < J_{2C}$, the ground state is unique and the excitation spectrum is gapless. At the critical value $J_{2C}=0.2411$,[15,16] a continuous phase transition of Kosterlitz-Thouless type into a gapped phase takes place. Here, the system breaks an Ising symmetry accompanied by bond order, i.e., spontaneous dimerization. At $J_2=0.5$, the so-called Majumdar-Ghosh (MG) point, the two ground-state wave functions are given by nearest-neighbor singlet product states:[17]

$$|0\rangle = [1,2][3,4][5,6]\ldots[2N-1,2N],$$

$$|\bar{0}\rangle = [2N,1][2,3][4,5]\ldots[2N-2,2N-1], \quad (2)$$

with $[i,j]$ denoting a normalized singlet combination of the spins at sites i and j,

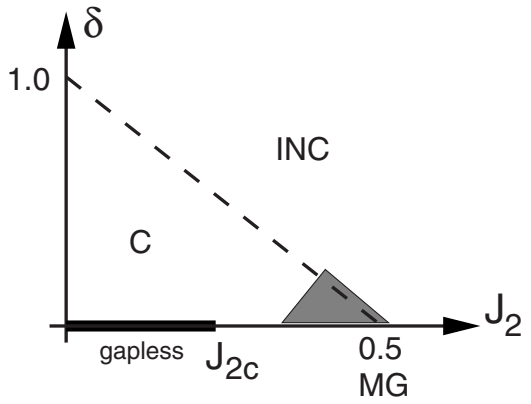

FIG. 2. Schematic ground-state phase diagram of the frustrated dimerized Heisenberg model (1). For $\delta=0$, the system is gapless for $J_2<J_{2C}=0.2411$ and spontaneously dimerized for $J_2>J_{2C}$, whereas $\delta>0$ induces a gap for all J_2. On the so-called disorder line, $2J_2+\delta=1$ (dashed), the ground state is given by a singlet product state on the strong bonds; moreover, the disorder line separates regimes of commensurate (C) and incommensurate (INC) spin correlations. The shaded area is the weakly confined regime of main interest in this paper, with $\xi_{\rm conf}\gg\xi_{\rm mag}$.

$$[i,j]=\frac{1}{\sqrt{2}}[|\uparrow\rangle_i|\downarrow\rangle_j-|\downarrow\rangle_i|\uparrow\rangle_j]. \tag{3}$$

The state $|0\rangle$ is illustrated in Fig. 1(b).

In the gapped phase, elementary excitations are topological defects (solitons or spinons) separating the states $|0\rangle$ and $|\bar{0}\rangle$. Shastry and Sutherland[18] performed variational calculations for the MG point using a reduced Hilbert space $\{|nm\rangle\}$, where the states $|nm\rangle$ consist of two spins at sites $2n-1$ and $2m$ separated by nearest-neighbor singlets, Fig. 1(c). It was shown that the low-lying excitations are pairs of propagating spinons, i.e., deconfined spin-1/2 (fractionalized) quasiparticles. The upper bound for the spinon dispersion, $\epsilon_k=(1/2)(5/4+\cos 2k)$, was later confirmed by numerical calculations.[19]

A finite dimerization δ opens a gap for all J_2. The perfectly dimerized states $|0\rangle$ and $|\bar{0}\rangle$ remain eigenstates of $H_{\rm ch}$ along the so-called "disorder line" $2J_2+\delta=1$, but their degeneracy is lifted by $\delta>0$. The energy of the ground state $|0\rangle$ is $E_0=(-3/8)(1+\delta)(2N)$. It was also shown that the static structure factor $S(q)=(1/2N)\Sigma_j\exp(iqR_j)\langle\mathbf{S}_0\cdot\mathbf{S}_j\rangle$ peaks at momentum $q=\pi$ and $q<\pi$, respectively, for points localized on the left (commensurate phase) and right (incommensurate phase) sides of the disorder line in the phase diagram.[13]

The fact that the states $|0\rangle$ and $|\bar{0}\rangle$ are no longer degenerate implies that the low-lying excitations are now bound states of two spinons, i.e., spin-1 confined objects.[19] Indeed, a finite value of δ introduces an effective attractive potential between two spinons: by converting one particular singlet of the state $|0\rangle$ into a triplet and then separating the two spinons as in the state $|nm\rangle$, the energy of the system increases by an amount proportional to $|m-n|\delta$. Such an increase is due to the fact the singlets between the two spinons are now located at the weak bonds [compare Figs. 1(a) and 1(c)].[20] As noted above, the spatial extension of the lowest-energy spinon-spinon bound state[21] provides a measure of the confinement length $\xi_{\rm conf}$, with $\xi_{\rm conf}\to\infty$ for $\delta\to 0$.

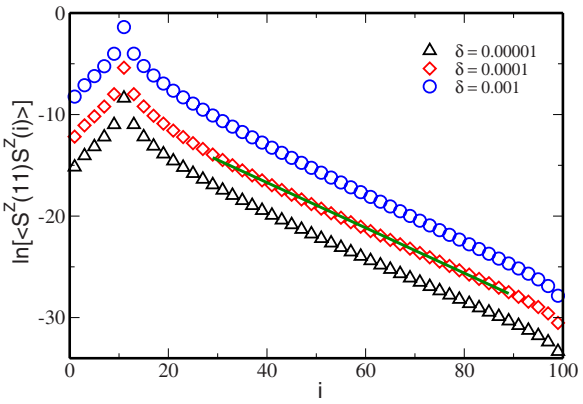

FIG. 3. (Color online) Natural logarithm of the spin-spin correlation function $\langle S^Z_{i=11}S^Z_i\rangle$ for $J_2=0.45$ and $\delta=10^{-5}$, 10^{-4}, and 10^{-3}. The results are from DMRG calculations with $m=128$ states for spin chain (1) with $2N=100$ sites. The curves are vertically shifted for visualization. Only the sites with $\langle S^Z_{i=11}S^Z_i\rangle>0$ are shown. The solid (green) line is an exponential fit to the data.

In the following, we shall be interested in the spin-gapped regime of weak confinement, with $\xi_{\rm conf}\gg\xi_{\rm mag}$. Thus we shall work at $\delta\ll 1$ and J_2 close to 1/2, Fig. 2. As the data analysis is much simpler for commensurate (instead of incommensurate) spin correlations, the regime to the right of the disorder line will be touched upon only briefly.

B. Methods

Ground-state properties of spin chain (1) will be calculated numerically for finite-size systems with the aid of the density-matrix renormalization group (DMRG) method,[22] using the libraries provided by the ALPS collaboration.[23] The calculations for $2N=100\ldots400$ sites employ open boundary conditions, such that strong bonds are located at the chain ends, Fig. 1(a).

In addition, near the disorder line, variational wave functions consisting of nearest-neighbor singlets with additional spinons will be utilized similar to those in Ref. 18. Details can be found in the Appendix.

III. SPIN CORRELATIONS OF UNDOPED SPIN CHAINS

As a reference, we calculate the bulk spin correlation function $\langle S^Z_iS^Z_j\rangle$ in the ground state of the Hamiltonian (1) using DMRG. We restrict our attention to small δ and the vicinity of the disorder line.

The typical behavior of $\langle S^Z_iS^Z_j\rangle$ within the bulk of the chain for $J_2=0.45$ and several values of δ is shown in Fig. 3 on a log-linear plot. One can clearly see an exponential decay of the spin correlations, i.e., $\langle S^Z_iS^Z_j\rangle\sim\exp(|i-j|/\xi_{\rm mag})$, as it is expected for a spin-gapped system. Similar results were found for $J_2=0.48$.

In Fig. 4, we show the values of $\xi_{\rm mag}$, obtained from an exponential fit to the long-distance part to the data, as a function of δ for $J_2=0.45$ and 0.48. (In the following, all

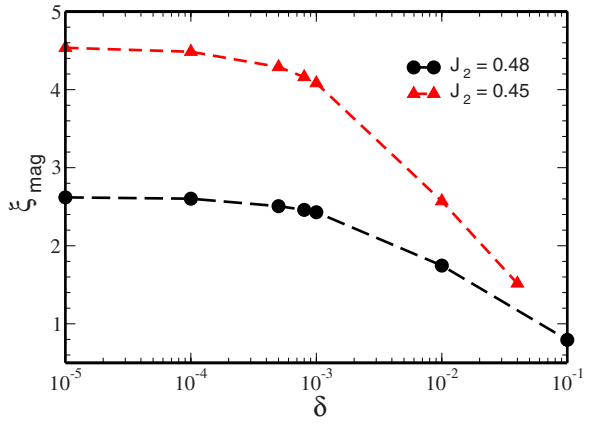

FIG. 4. (Color online) The magnetic correlation length for $J_2=0.45$ and $J_2=0.48$ in terms of δ calculated via DMRG (see text for the details of the calculation). The dashed lines are guide for the eyes.

length scales are measured in units of the lattice spacing.) For a fixed value of J_2, ξ_{mag} increases as the dimerization decreases and then approaches a constant value in the limit $\delta \to 0$. ξ_{mag} increases as J_2 is reduced for a fixed value of δ. This behavior is in agreement with the discussions of Sec. II. Recall that along the line $\delta=0$, ξ_{mag} diverges as $J_2 \to J_{2C}$ from above. We note that *on* the disorder line ξ_{mag} is minimal, but the correlations cannot be reasonably fitted to an exponential decay, as the ground state of the infinite system is given by the product state $|0\rangle$ [Eq. (2)].

IV. SPIN CHAINS WITH A NONMAGNETIC IMPURITY

Vacancy doping in quantum paramagnets can induce effective magnetic moments. These impurity-induced moments reveal themselves in a Curie-type behavior of the uniform susceptibility, $\chi \propto C/T$, at intermediate temperatures. Remarkably, in the presence of three-dimensional couplings these induced moments can order at sufficiently low temperatures, thus changing the spin-gapped paramagnetic ground state of the pure compound into a magnetically long-range-ordered state upon doping.

The appearance of effective moments upon doping vacancies is a property of systems with confined spinons; for spin-1/2 systems it is best visualized in terms of broken singlet bonds where one spin is replaced by a vacancy. The liberated spin 1/2 is confined to the vacancy at low energies resulting in an effective spin-1/2 moment.[24,25] In contrast, in host systems with deconfined spinons, no moments are generated by introducing vacancies. This theoretical picture has been supported by various numerical studies, in particular on spin chain[26] and ladder systems.[27–29]

In the following, we present analytical and DMRG results for spin chains with a single vacancy, with focus on the spin polarization cloud associated with the impurity-induced magnetic moment. It has been established that, in the strongly confined regime, the cloud consists of excited triplets, with the spatial size given by ξ_{mag}.[27–31] In contrast, in the weakly confined regime the cloud size is given by the

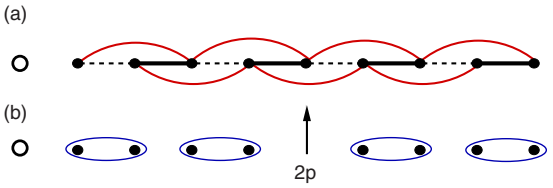

FIG. 5. (Color online) Schematic representation of (a) Hamiltonian (1) with a nonmagnetic impurity (open circle) at site $i=1$ and (b) the state $|p\rangle$ which consists of an empty site at $i=1$ and a spinon at site $2p$ separated by a singlet pattern. The symbols are the same as in Fig. 1.

extension of the spinon-holon bound state, i.e., ξ_{conf}. Indeed, we shall find a cloud of size $\max(\xi_{\mathrm{mag}}, \xi_{\mathrm{conf}})$, with a distinct crossover for $\xi_{\mathrm{mag}} \sim \xi_{\mathrm{conf}}$. The shape of the spin polarization cloud allows us to distinguish the weakly from the strongly confined regime.

A remark on limits is in order here: the ground state of the infinite system with a single vacancy is doubly degenerate corresponding to the residual vacancy-induced moment. Applying a uniform field $h_u \ll \Delta$, where Δ is the bulk spin gap, fully polarizes this moment and leads to a static staggered spin arrangement near the vacancy. A finite concentration of vacancies introduces another energy scale, namely, the effective (maximum) interimpurity interaction J_{eff}; see also Sec. V C. The following discussion of the polarization cloud around a vacancy assumes the limit $h_u \to 0$, keeping $J_{\mathrm{eff}} \ll h_u \ll \Delta$.

A. Variational calculations

Near the disorder line the low-energy states of the dimerized spin chain (1) are dominated by short-range singlet coverings: The $S=1$ states $|mn\rangle$, Fig. 1(c), have a lower energy than any $S=2$ state even for a large separation $(m-n)$ between the two spinons. This is the basis of the variational method of Ref. 18, which we adopt here to calculate the spin correlations in the vicinity of a nonmagnetic impurity.

Consider the frustrated dimerized spin chain (1) with strong bonds at the chain ends and introduce a vacancy at an odd site. For finite dimerization, $\delta>0$, the system has no inversion symmetry at the impurity site i_{imp} even in the infinite-system limit. In this configuration, the liberated spin 1/2 stays mainly in the region $i>i_{\mathrm{imp}}$: recall that the low-energy sector is formed by states made out of short-range singlets. The free spin can only occupy a site $i<i_{\mathrm{imp}}$ if a (long) singlet is formed between the spins at sites $i_{\mathrm{imp}}-1$ and $i_{\mathrm{imp}}+1$, which corresponds to a high-energy state. To simplify the variational calculations, we shall therefore ignore the region $i<i_{\mathrm{imp}}$, i.e., consider a spin chain with the vacancy placed at the chain end, as illustrated in Fig. 5(a). Also, we focus on parameter values on the disorder line, $J_2=(1-\delta)/2$ with $10^{-5} \le \delta \le 10^{-2}$.

We restrict the variational Hilbert space to the states $|p\rangle$, which consist of an empty site at $i=1$ and a spinon at site $2p$ in a background of nearest-neighbor singlets as illustrated in Fig. 5(b). The states $|p\rangle$ are not orthogonal to each other. In fact, the overlap between two states $|m\rangle$ and $|p\rangle$ reads

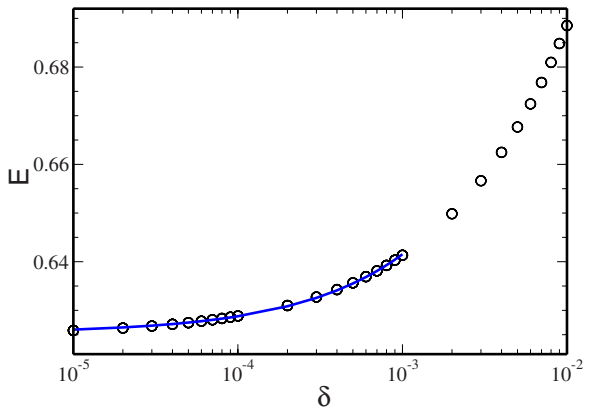

FIG. 6. (Color online) Variational ground-state energy E as a function of δ (open circles) for the doped frustrated dimerized spin chain. The results are for points along the disorder line, i.e., $J_2=(1-\delta)/2$. The solid (blue) line is a power-law fit to the data in the region $10^{-5}\leq\delta\leq 10^{-3}$ (see text for details).

$$\langle m|p\rangle = \left(-\frac{1}{2}\right)^{|m-p|}. \tag{4}$$

A long but straightforward calculation shows that the matrix elements of the Hamiltonian (1) with a vacancy at site $i=1$ are given by

$$\begin{aligned} 2\langle m|H-E_0|p\rangle = \frac{1}{2}\{2+5J_2+3(1-2J_2)[1+\theta_+(m,p) \\ +(m-p)\theta_-(m,p)]+3\delta[2p-1+\theta_-(m,p) \\ +(m-p)\theta_+(m,p)]\}\langle m|p\rangle+(1+\delta-J_2) \\ \times\langle m|p-1\rangle+(1-\delta-J_2)\langle m|p+1\rangle, \end{aligned} \tag{5}$$

where $E_0=-(3/8)(1+\delta)(2N)$, $\theta_+(m,p)\equiv\theta(p-m-1)+\theta(m-p-1)$, and $\theta_-(m,p)\equiv\theta(p-m-1)-\theta(m-p-1)$ with the step function $\theta(x)$ defined as in Eq. (A8).

Instead of considering the nonorthogonal basis $\{|p\rangle\}$, we can define a orthonormal one[20] via the Gram-Schmidt orthogonalization procedure, namely,

$$|\phi_1\rangle \equiv |1\rangle,$$

$$|\phi_p\rangle = \frac{2}{\sqrt{3}}[|p\rangle+(1/2)|p-1\rangle], \quad p\geq 2. \tag{6}$$

Diagonalizing the Hamiltonian (5) in the basis $\{|\phi_p\rangle\}$ gives the ground-state energy E and wave function $|\Psi\rangle$ in the presence of an impurity:

$$|\Psi\rangle = \sum_{p=1}^{N} C_p|\phi_p\rangle. \tag{7}$$

In Fig. 6, we show the energy E as a function of δ calculated for a spin chain with $2N=600$ sites using the procedure described above. The data in the region $10^{-5}\leq\delta\leq 10^{-3}$, which, as we will see in the next section, is deep in the weakly confined regime, can be fitted by a power law $a_0+a_1\delta^{2/3}$ with $a_0=0.6252$ and $a_1=1.6241$. Such δ dependence of the ground-state energy is chosen based on the analytical findings of Uhrig *et al.*,[20] who studied a similar problem via an effective one-dimensional Schrödinger equation. They showed that the solutions $\psi(x)$ of the effective equation can be written as $\psi(x)\sim \mathrm{Ai}(x/\xi+z_i)$, where z_i are the zeros of the Airy function $\mathrm{Ai}(x)$ (Ref. 32) and $\xi=(3m\delta/2)^{-1/3}$ is the characteristic length scale with m being the spinon mass, and the ground-state energy $E\sim\delta^{2/3}$.

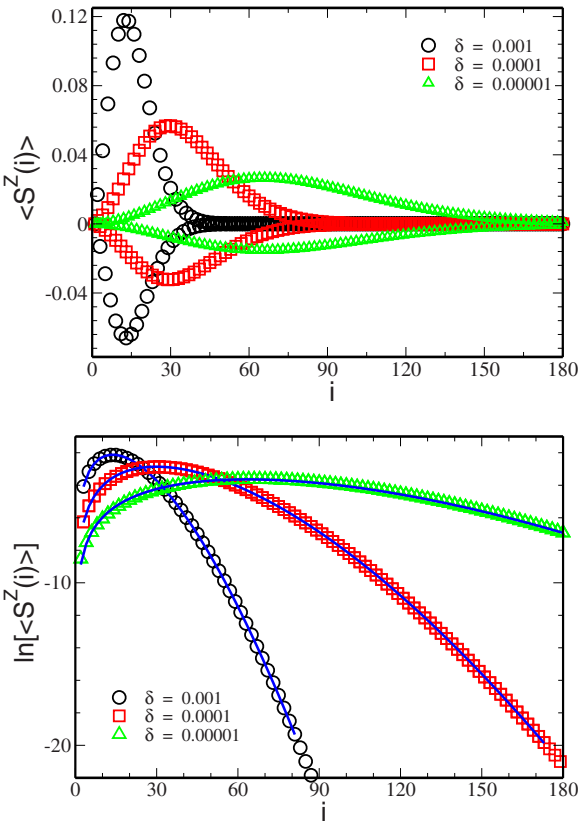

FIG. 7. (Color online) Variational results for the spin polarization $\langle S_i^Z\rangle$ around $i_{\mathrm{imp}}=1$. $J_2=(1-\delta)/2$ and $\delta=10^{-3}$ (black circles), 10^{-4} (red squares), and $\delta=10^{-5}$ (green triangles). Top panel: linear-linear scale. Bottom panel: same data on a log-linear scale showing only the sites with $\langle S_i^Z\rangle>0$; the solid (blue) lines are fits to the data using Eq. (9) for the entire data set with $i>1$ and $\ln[\langle S_i^Z\rangle]>-20$.

Once the coefficients C_p are known, the spin polarization $\langle S_i^Z\rangle=\langle\Psi|S_i^Z|\Psi\rangle=\Sigma_{p,m}C_m^*C_p\langle\phi_m|S_i^Z|\phi_p\rangle$ can be calculated with the aid of Eq. (6) and the expression

$$\begin{aligned} \langle m|S_i^Z|p\rangle = (-1)^i\frac{1}{2}[\theta(i-2m)\theta(2p-i)+\theta(i-2p)\theta(2m-i)] \\ \times[1-(1/2)\delta_{m,p}]\langle m|p\rangle. \end{aligned} \tag{8}$$

The results for $\delta=10^{-5}\ldots 10^{-3}$ are shown in Fig. 7 on linear-linear and log-linear scales. One can see that the spin polarization has a staggered profile in the vicinity of i_{imp} as is was already realized in previous calculations.[19,28,33] By decreasing the dimerization, not only the position of the maximum of $\langle S_i^Z\rangle$ moves away from the impurity site but also the distribution gets broader and broader. Such features indicate that the system approaches a deconfined regime as the dimer-

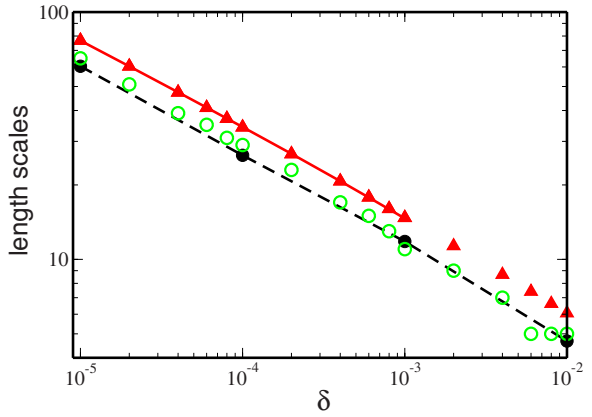

FIG. 8. (Color online) Variational ξ_{cm} (filled red triangles), ξ_{max} (open green circles), and ξ_1 (filled black circles) as a function of δ for the disorder line. The solid (red) line corresponds to a power-law fit to the data in the region $10^{-5} \leq \delta \leq 10^{-3}$ (see text for details) and the dashed line is a guide for the eyes.

ization decreases. Indeed, at $\delta=0$, the spin polarization peaks at the center of the chain.

We now discuss possible quantitative measures of the size of the polarization cloud. This is not trivial, as the long-distance decay deviates from a pure exponential, in particular for small δ. The asymptotic behavior of the Airy function $\mathrm{Ai}(x)$ suggests a fit using the expression

$$\log\langle S_i^Z\rangle = b_1 - [|i-i_{\mathrm{imp}}|/\xi_1]^{1+b_3^2} + b_2 \log|i-i_{\mathrm{imp}}| \qquad (9)$$

for $i > i_{\mathrm{imp}}$, with parameters $b_{1\ldots3}$ and ξ_1, the latter being the length scale corresponding to the cloud size. This formula, being able to interpolate between a pure exponential and a faster decay, depending on whether $b_3=0$ or $b_3\neq 0$, nicely fits the data as is illustrated in Fig. 7. Alternative definitions for the polarization cloud size (to the right of i_{imp}) are given by the position of the maximum ξ_{max} of $\langle S_i^Z\rangle$ relative to i_{imp} and by the center-of-mass coordinate of the cloud:[34]

$$\xi_{\mathrm{cm}} = \frac{\sum_{i=1}^{2N} (i-i_{\mathrm{imp}})|\langle S_i^Z\rangle|}{\sum_{i=1}^{2N} |\langle S_i^Z\rangle|}. \qquad (10)$$

The variational results for ξ_{cm}, ξ_{max}, and ξ_1 as a function of δ are plotted in Fig. 8. As expected, the cloud size diverges as $\delta\to 0$, which corresponds to the MG point, and all measures are much larger than $\xi_{\mathrm{mag}}\sim 1$. For instance, the data for ξ_{cm} in the region $10^{-5}\leq\delta\leq 10^{-3}$ can be fitted by $a_0+a_1\delta^{-1/3}$ with $a_0=-2.3952$ and $a_1=1.7031$. Again, the δ dependence follows from the results derived in Ref. 20.

B. Numerical results

We now use DMRG to investigate spin chains with a single vacancy in a parameter regime away from the disorder line. We keep $m=150$ states for a chain with $2N=400$ sites and open boundary condition, and the vacancy is located at site $i_{\mathrm{imp}}=101$, Fig. 9(a). This choice is due to the fact that the

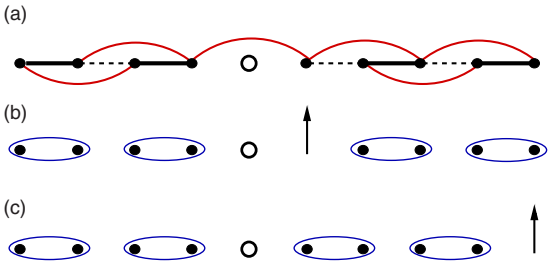

FIG. 9. (Color online) Schematic representation of (a) Hamiltonian (1) with a nonmagnetic impurity (open circle) at site i_{imp} and the ground-state configurations for (b) strongly and (c) weakly confined regimes. The symbols are the same as in Fig. 1.

spin polarization cloud around i_{imp} is asymmetric (see the discussion below). In the following, we only discuss the properties of lowest state in the $S_{\mathrm{tot}}^Z=-1/2$ sector.

Some representative results for the spin polarization around the vacancy are plotted in Fig. 10 on a log-linear scale (only $\langle S_i^Z\rangle>0$ are shown). For the disorder line, the spin polarization curves are asymmetric with respect to i_{imp}. On the left side of the impurity ($i<i_{\mathrm{imp}}$) an exponential tail is evident while on the right side ($i>i_{\mathrm{imp}}$) the shape of the spin polarization resembles the one described in the last section. In fact, the results of DMRG and the variational ap-

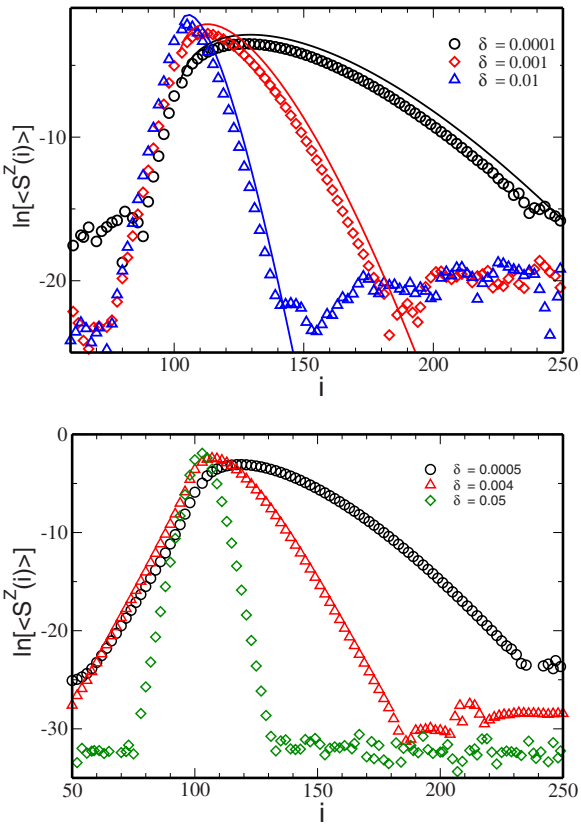

FIG. 10. (Color online) DMRG results for the spin polarization $\langle S_i^Z\rangle$ around the vacancy in the $J_1-J_2-\delta$ chain, for parameters on the disorder line (top panel) and for $J_2=0.48$ (bottom panel). The system size is $2N=400$ and the vacancy is at site $i=101$. Only the sites with $\langle S_i^Z\rangle>0$ are shown. The solid lines in the top panel are the variational results calculated in Sec. IV A.

proach (solid lines in Fig. 10) are in quite good agreement. The behavior for the $J_2=0.48$ line is richer: notice that for the largest value of δ, $\langle S_i^Z\rangle$ is symmetric around the impurity site with exponential tails. As δ decreases, the curves become more and more asymmetric, i.e., they display features qualitatively similar to the ones observed for the disorder line. Indeed for $\delta<10^{-2}$ a pure exponential decay is no longer visible in the region $i>i_{\mathrm{imp}}$. Similar behavior (not shown here) is observed for $J_2=0.45$. We have also studied the vacancy-induced spin polarization for $J_2>1/2$: in this regime, the polarization displays incommensurate oscillations with an envelope similar to those in Fig. 10. However, the incommensurate behavior complicates numerical fits such that we refrain from a further analysis.

We proceed as in Sec. IV A and perform a quantitative analysis of the DMRG data for $\langle S_i^Z\rangle$. Our results are summarized in Fig. 11, which shows the decay lengths ξ_1, ξ_2 (described below), the center-of-mass position of the cloud, ξ_{cm} [Eq. (10)], and the bulk correlation length ξ_{mag} (Sec. III) as function of δ for three different values of J_2. We also include the variational ξ_{cm} determined in the previous section. One can see that the variational and DMRG results for ξ_{cm} along the three lines are in quite good agreement. This implies that the restriction of the Hilbert space to the subspace $\{|p\rangle\}$ is a reasonable approximation to describe the (weak) confinement physics. Recall that $|p\rangle$ includes only singlets made out of neighboring sites and the ones between the i_{imp} and the spinon site are located at the weak bonds in contrast to the ground state of the *undoped* chain whose singlet pairs are placed at the strong bonds.

The spatial decay of the spin polarization cloud, $\langle S_i^Z\rangle$, can be analyzed with the aid of expression (9). As $\langle S_i^Z\rangle$ is asymmetric due to the broken inversion symmetry with respect to i_{imp}, we use Eq. (9) separately for the regions $i>i_{\mathrm{imp}}$ and $i<i_{\mathrm{imp}}$ to extract the length scales ξ_1 and ξ_2, respectively. In both cases, we only include data points into the fit where $\langle S_i^Z\rangle$ is above the noise floor of the numerical data, e.g., $i_{\mathrm{imp}}<i<140$ in the ξ_1 fit of the $\delta=0.01$ data in the top panel of Fig. 10. The ξ_1 and ξ_2 resulting from the fit are shown in Fig. 11 as well.

Let us discuss the results collected in Fig. 11. In all panels, one can identify three distinct regimes: (a) For large δ, we have $\xi_1\approx\xi_2\approx\xi_{\mathrm{mag}}$, i.e., both parts of the spin polarization cloud are determined by magnetic (bulk) correlations. We identify this as the strongly confined regime. (b) For small δ, $\xi_1\approx\xi_{\mathrm{cm}}\gg\xi_2\approx\xi_{\mathrm{mag}}$. Hence, the right part of the polarization cloud is determined by the confinement length, which is moreover much larger than the bulk correlation length. These are characteristics of the weakly confined regime, and we conclude $\xi_1=\xi_{\mathrm{conf}}$. (c) There is a pronounced crossover regime between (a) and (b), e.g., $10^{-3}\lesssim\delta\lesssim10^{-2}$ for $J_2=0.48$. As anticipated above, ξ_{conf} diverges as $\delta\to0$ while ξ_{mag} approaches a constant value—this proves the existence of two length scales in the regime of weak confinement.

Qualitatively, the behavior of the spin polarization cloud is easily understood: for strong confinement, i.e., large δ, we have $\xi_{\mathrm{conf}}\sim1$, which implies that the spinon is close to i_{imp}. Figure 9(b) illustrates the most probable configuration of the ground state. Notice that the singlet pairs are at the strong bonds as in the ground state of the *undoped* chain. Therefore the enhancement of the spin correlations around i_{imp} is mainly due to triplets that are excited by the coupling between the spin adjacent to the impurity (i.e., the spinon) and the environment.[27–31] The triplet physics is dominated by ξ_{mag}, hence $\xi_1\approx\xi_2\approx\xi_{\mathrm{mag}}$. On the other hand, in a weakly confined regime of small δ, $\xi_{\mathrm{conf}}\gg1$. The spinon travels to distant sites $i>i_{\mathrm{imp}}$, Fig. 9(c), where it may also generate

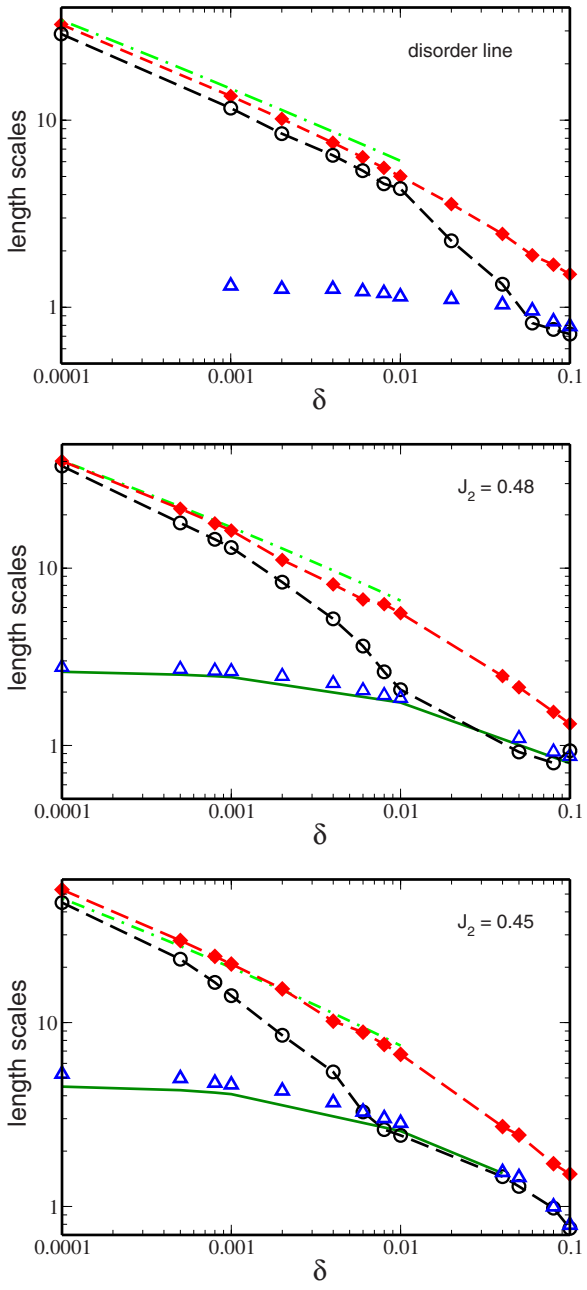

FIG. 11. (Color online) The characteristic length scales ξ_1 (open circles) and ξ_2 (open triangles), ξ_{cm} (diamonds), and ξ_{mag} (solid line) as function of δ for $J_2=(1-\delta)/2$, 0.48, 0.45 from top to bottom, extracted from DMRG (see text for details). The variational ξ_{cm} (dashed-dotted line) is also shown for comparison. The dashed lines are guide for the eyes. Note that (i) ξ_{mag} cannot be meaningfully defined for $J_2=(1-\delta)/2$, i.e., on the disorder line, and that (ii) $J_2=0.48$ and $\delta>0.04$ corresponds to the incommensurate region.

triplets. In contrast, configurations with the spinon at sites $i < i_{\mathrm{imp}}$ are suppressed as they require a long, i.e., high-energy, singlet. Hence, the impurity-induced spin polarization for $i > i_{\mathrm{imp}}$ profits from the traveling spinon and is determined by ξ_{conf} (provided that $\xi_{\mathrm{conf}} > \xi_{\mathrm{mag}}$) whereas the polarization for $i < i_{\mathrm{imp}}$ decays on the bulk scale ξ_{mag}.

To summarize, the size and shape of the spin polarization induced by a nonmagnetic impurity allow to distinguish the regimes of weak and strong confinement. In the present 1D case, both length scales ξ_{conf} and ξ_{mag} can in principle be extracted from $\langle S_i^Z \rangle$.

V. WEAK CONFINEMENT IN EXPERIMENTS

In this section, we briefly sketch how weak confinement manifests itself in standard experiments. As before, the discussion is focused on 1D systems but qualitatively applies to $D \geq 2$ as well; see Sec. VI.

A. Dynamic susceptibility: Multiple bound states

We start with the zero-temperature dynamic susceptibility $\chi(\vec{q}, \omega)$ of a clean (i.e., impurity-free) gapped confined paramagnet. The minimum of the triplon dispersion is located at some wave vector $\vec{q} = \vec{Q}$, where $\chi(\vec{q}, \omega = 0)$ displays a maximum.

In the conventional case of strong confinement, $\chi''(\vec{Q}, \omega)$ consists of a single sharp peak at the spin-gap energy Δ, corresponding to the triplon particle, and a continuum of multiparticle states, which typically starts at 3Δ. (In low-symmetry situations, such as the $J_1 - J_2 - \delta$ chain, a two-particle continuum starting at 2Δ at $\vec{q} = \vec{2}Q$ is present.) In contrast, in a situation of weak confinement, there will be additional sharp peaks between Δ and the onset of the continuum. This can be easily understood: while Δ is the energy of the lowest spin-1 two-spinon bound state, weak confinement implies that higher two-spinon bound states are energetically only slightly above Δ. The crossover to strong confinement may be defined by the criterion that Δ becomes equal to the energetic difference between the two lowest $S = 1$ two-spinon states.

For the $J_1 - J_2 - \delta$ chain considered above, the dynamic structure factor has been discussed, e.g., in Ref. 35. The energy spacing of the two-spinon bound states scales as $\delta^{-2/3}$, i.e., the number of bound states below the continuum diverges as $\delta \to 0$. The precise structure of $\chi''(\vec{Q}, \omega)$ is determined by the energies and matrix elements of the two-spinon bound states, the latter giving the weights of the peaks in χ''. The energies depend on the bound state number n as $\Delta + n^{2/3}$. Reference 35 also provides an estimate of the peak weights, but the employed continuum limit is questionable because the weight depends on the short-distance behavior of the two-particle wave function, which is strongly influenced by lattice effects due to the nonanalytic nature of the confinement potential $V(x) = \alpha|x|$. Numerical results for $\chi''(\vec{q}, \omega)$ in the $J_1 - J_2 - \delta$ chain can be found in Refs. 19 and 36–38, which clearly show additional sharp modes below the continuum. In particular, Fig. 4 of Ref. 36 reports energies of *triplon* bound states on the disorder line for $\delta = 0.4$. As both single-triplon states and two-triplon spin-1 bound states correspond to two-spinon spin-1 bound states, their results can be directly cast in our language: there are two (four) two-spinon spin-1 bound states below the two-particle continuum at wave vector 0 ($\pi/2$), but already the second is very close to the lower edge of the continuum, consistent with $\delta = 0.4$ being located in the crossover regime between weak and strong confinement, Fig. 11.

B. NMR line shape due to vacancies

We now return to confined paramagnets doped with nonmagnetic impurities, which generate a spin polarization cloud as discussed in detail in Sec. IV. This spin polarization can be made static by applying an external field larger than the interimpurity interaction (see Sec. V C below). The method of choice would be spin-resolved scanning tunneling microscopy imaging of the cloud which, however, is not readily available with atomic resolution. Alternatively, nuclear magnetic resonance provides a tool to detect the distribution of local fields. For instance, for doped antiferromagnetic spin chains,[39] a broadening of the NMR spectrum at very low temperatures is observed while, for a doped Haldane chain, the satellite peaks in the NMR spectrum even allow the experimental determination of the magnetic correlation length.[40]

The Knight shift K_i of the resonance field at the site i is proportional to the local electronic moment (omitting the factor of the electron-nucleus hyperfine coupling); the NMR spectrum simply corresponds to the distribution of the local shifts K_i. We are interested in the staggered component of the polarization, which can be defined in 1D as[34]

$$\langle S_i^Z \rangle_{\mathrm{stag}} = \frac{1}{4}(-1)^i [2\langle S_i^Z \rangle - \langle S_{i+1}^Z \rangle - \langle S_{i-1}^Z \rangle]. \tag{11}$$

For the spin chain of Sec. IV B, we calculate the distribution of staggered Knight shifts using

$$I(x) = \sum_{i=1}^{2N} f_\epsilon [x - \langle S_i^Z \rangle_{\mathrm{stag}}], \tag{12}$$

where $f_\epsilon(x)$ is chosen as a Lorentzian with a small width ϵ in order to have a smooth $I(x)$ curve.

In Fig. 12 we show examples of the NMR spectrum calculated using Eq. (12) and the DMRG results derived in Sec. IV B for a chain with a single impurity. The results are for $J_2 = 0.48$ and $\delta = 0.0001$, 0.004, and 0.04, which are in the regions of weak, intermediate, and strong confinement, respectively. As it was already observed in Ref. 28 the main effect is the broadening of the spectral line.

Weak confinement leads to an asymmetric spectrum with a pronounced shoulder for one sign of x. This asymmetry is directly related to the spatial asymmetry of the spin polarization cloud and can be understood as follows: for an impurity as in Fig. 9, sites with $i > i_{\mathrm{imp}}$ ($i < i_{\mathrm{imp}}$) have $\langle S_i^Z \rangle_{\mathrm{stag}} < 0$ ($\langle S_i^Z \rangle_{\mathrm{stag}} > 0$), respectively. Hence, the part of the cloud dominated by weak confinement, $i > i_{\mathrm{imp}}$, contributes to $I(x < 0)$, where the large extension of the cloud results in a prominent tail of $I(x < 0)$. Obviously, for a finite concentration of im-

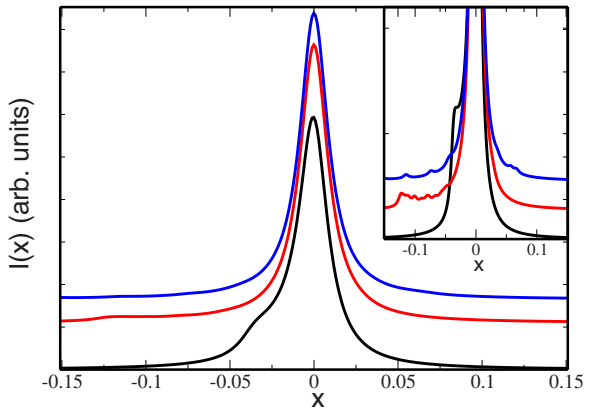

FIG. 12. (Color online) Distribution function $I(x)$ (NMR spectrum) with broadening $\epsilon=0.02$ for $J_2=0.48$ and several values of δ calculated using the DMRG results of Sec. IV B. The curves are vertically shifted for better visualization. From bottom to top we have $\delta=0.0001$ (black), 0.004 (red), and 0.04 (blue). Inset: $I(x)$ with a smaller broadening $\epsilon=0.01$.

purities, evenly distributed on both sublattices, the asymmetry of the line shape will disappear, but the shoulder feature remains.

C. Effective interaction between vacancy-induced moments

In the experimentally relevant situation of a finite concentration of nonmagnetic impurities, the induced moments couple via an indirect exchange interaction mediated by the gapped host. If the underlying lattice is bipartite, then the arising magnetism is typically nonfrustrated despite the strong disorder inherent to the problem. In $D=3$ and at sufficiently low temperatures, this interaction may lead to impurity-induced magnetic order in the paramagnetic host. Experimentally, this phenomenon has been observed in a variety of magnets, e.g., Zn-doped $CuGeO_3$,[41–43] Zn-doped $SrCu_2O_3$,[44] and Mg-doped $TlCuCl_3$.[45]

On the theoretical side, vacancy-induced magnetic ordering in such compounds is commonly described by effective models, which exclusively contain the impurity-induced moments of spin 1/2, which are the only low-energy degrees of freedom below the bulk spin gap (for small impurity concentration). The coupling between these moments is written down as a Heisenberg-type model, with spins S_i at the random impurity locations, and a pairwise exchange coupling J_{ij} of the form

$$J_{ij} \propto (-1)^{r_{ij}} \exp(-r_{ij}/\xi_{\mathrm{mag}}). \tag{13}$$

Here r_{ij} is the distance between two impurities at sites i and j. Note that the common assumption is that the decay length of the J_{ij} is the bulk correlation length ξ_{mag}.

In the following, we argue that Eq. (13) does not apply to the regime of weak confinement: there, the decay length of the J_{ij} is given by ξ_{conf} instead. The simplest argument is that J_{ij} is determined by the overlap between the spin polarization clouds associated with the vacancies at sites i and j. As shown above, the cloud size crosses over from ξ_{mag} in the strongly confined regime to ξ_{conf} in the weakly confined regime—the same now applies to the decay length of the J_{ij}.

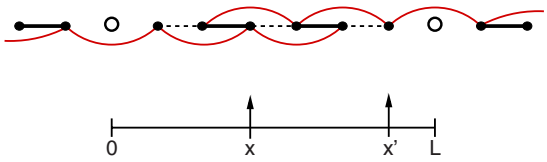

FIG. 13. (Color online) Schematic representation of Hamiltonian (1) with two nonmagnetic impurities (top panel) and two spinons between two impurities separated by a distance L (bottom panel). The symbols are the same as in Fig. 1.

To make this explicit, let us consider the spin chain described by the Hamiltonian (1) with two vacancies, the first one located at an odd site and the second at an even site, as illustrated in Fig. 13. In this configuration, the two spinons stay mainly in the region of size L between the two impurities. As for the strongly confined regime, we assume that in the ground state the two spinons are in a singlet configuration with energy $E^0_{S=0}$ and define the effective exchange coupling as

$$J^{\mathrm{eff}} = E^0_{S=1} - E^0_{S=0}, \tag{14}$$

where $E^0_{S=1}$ is the energy of the lowest triplet configuration.[34]

We proceed along the lines of Refs. 20 and 35 and study the two-impurity problem near the disorder line via an effective Schrödinger equation in the continuum limit, which captures the physics in the Hilbert space sector without excited triplets. The continuum limit is justified here, as the effective interaction turns out to be dominated by the long-distance tail of the wave function. Within this approach, the difference between the singlet and the triplet configurations is given by the boundary conditions imposed on the total wave function $\Psi(x,x')$. For the triplet configuration, the two spinons are not allowed to penetrate through each other while such process is permitted for the singlet one. Moreover, if we assume that the total wave function can be written as a product, i.e., $\Psi(x,x') \sim \psi(x)\psi(x')$, then we can reduce the two-particle problem to a single-particle one. Such considerations lead us to describe a spinon of mass m at position x by the Schrödinger equation

$$E\psi(x) = -\frac{J}{2m}\frac{\partial^2}{\partial x^2}\psi(x) + \frac{3\delta J}{4}x\psi(x), \tag{15}$$

subject to the following boundary conditions:

$$\text{singlet: } \psi^s(x=0) = \psi^s(x=L) = 0, \tag{16}$$

$$\text{triplet: } \psi^t(x=0) = \psi^t(x=L/2) = 0. \tag{17}$$

Notice that Eq. (16) reflects the fact that the motion of the spinon is restricted to the region between the two impurities while the second term of Eq. (17) simulates the nonpenetration condition for the triplet configuration.

The differential equation (15) has an analytical solution given in terms of a linear combination of shifted Airy functions $\mathrm{Ai}(x)$ and $\mathrm{Bi}(x)$, i.e.,[32]

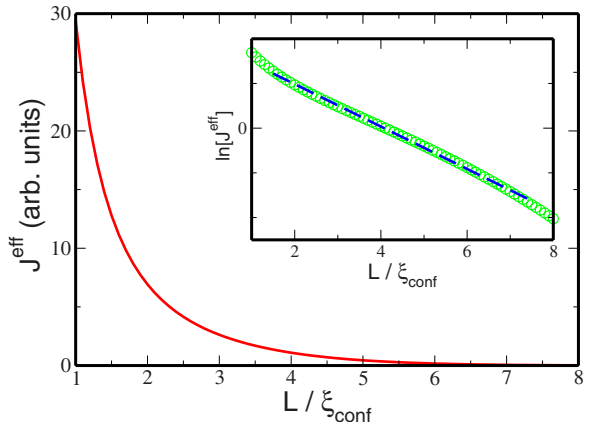

FIG. 14. (Color online) Effective exchange coupling J^{eff} [Eq. (14)] as a function of the renormalized impurity-impurity distance L/ξ_{conf}. Inset: natural logarithm of J^{eff} (open green circles) and the corresponding linear fitting (dashed blue line).

$$\psi(x) = \alpha \text{Ai}(x/\xi + x_0) + \beta \text{Bi}(x/\xi + x_0), \tag{18}$$

with the corresponding eigenvalue

$$E = -\frac{Jx_0}{2m\xi^2}. \tag{19}$$

Based on the discussions on Sec. IV A, $\xi=(3m\delta/2)^{-1/3}$ is identified with ξ_{conf}. x_0 is determined from the boundary conditions (16) and (17), more precisely, from the solutions of the following equation:

$$\text{Bi}(x_0)\text{Ai}(l + x_0) - \text{Ai}(x_0)\text{Bi}(l + x_0) = 0, \tag{20}$$

with $l=L/\xi_{\text{conf}}$ (singlet) and $l=L/(2\xi_{\text{conf}})$ (triplet). We solve Eq. (20) numerically, calculate the corresponding effective exchange coupling as a function of L/ξ_{conf} according to Eq. (14), and plot the result in Fig. 14. One can see that J^{eff} decays exponentially with the renormalized impurity-impurity distance L/ξ_{conf}. Indeed, the log-linear data in the inset of Fig. 14 can be fitted by $\ln(J^{\text{eff}})=a_0-a1(L/\xi_{\text{conf}})$ with $a_0=3.8681$ and $a_1=0.9491$. As the calculation applies to a parameter regime of the spin chain where the bulk correlation length is of order unity, this shows that the effective interaction follows Eq. (13) with the replacement $\xi_{\text{mag}} \to \xi_{\text{conf}}$.

D. Vacancy-induced order: Staggered magnetization

In a situation where the effective interaction discussed above leads to long-range magnetic order, the staggered magnetization, being the order parameter, will be strongly inhomogeneous. Nevertheless, the Bragg peak seen in the elastic neutron-scattering signal at the ordering wave vector $\vec{Q}$ will be proportional to the *total* staggered magnetization of the system. For dilute impurities and neglecting fluctuation effects, this is just given by the number of impurities times the staggered magnetization per impurity, M_{stag}. Note that this quantity can be much larger than 1/2, in contrast to the uniform moment associated with each impurity which equals 1/2.

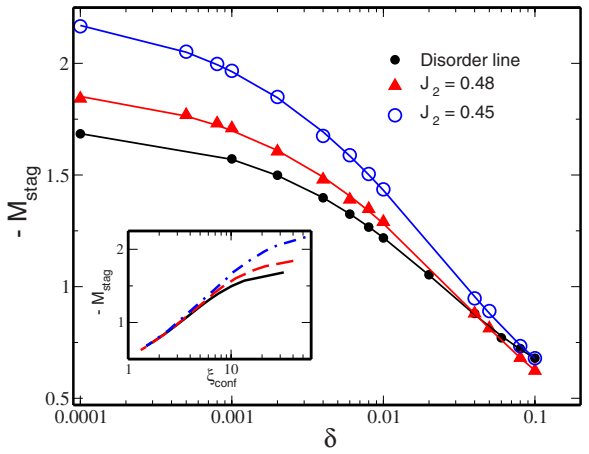

FIG. 15. (Color online) The total staggered magnetization associated with one impurity as a function of δ for the disorder, $J_2=0.48$ and 0.45 lines calculated using the DMRG results of Sec. IV B. The solid lines are fitted to the data (see text for details). Inset: M_{stag} in terms of ξ_{conf}. Results for the disorder (solid black line), $J_2=0.48$ (dashed red line), and $J_2=0.45$ (dashed-dotted blue line) lines.

In the following, we calculate the staggered magnetization

$$M_{\text{stag}} = \sum_{i=1}^{2N} (-1)^i \langle S_i^Z \rangle, \tag{21}$$

for a spin chain with a single vacancy from the DMRG data of Sec. IV B. The behavior of M_{stag} as a function of δ for the disorder, $J_2=0.48$ and 0.45 lines is displayed in Fig. 15. One can see that $|M_{\text{stag}}|$ increases as we move into the weakly confined regime but does *not* diverge in the limit $\delta \to 0$, despite the diverging cloud size, $\xi_{\text{conf}} \to \infty$, in this limit. Indeed, by fitting the curves with the expression

$$-M_{\text{stag}}(\delta) = c_0 + c_1 \exp(-c_2 \delta^{c_3}),$$

we find that $M_{\text{stag}}(\delta \to 0)=1.7275$, 1.9186, and 2.2648, respectively, for the disorder, $J_2=0.48$, and 0.45 lines.

The finite value of M_{stag} as $\xi_{\text{conf}} \to \infty$ is to be contrasted with the situation of an impurity near a magnetic quantum critical point in $2 \le D \le 4$, where $\xi_{\text{mag}} \to \infty$ leads to $M_{\text{stag}} \to \infty$.[30] Again, the difference can be understood within the picture developed above: on the one hand, for $\xi_{\text{conf}} \to \infty$ and finite ξ_{mag}, the polarization cloud is primarily made out of many magnetically neutral singlets, see Fig. 9. Indeed, in this case, it is possible to show analytically[20] that M_{stag} approaches a constant as $\delta \to 0$. (This constant, however, depends on ξ_{mag}, see Fig. 15.) On the other hand, for $\xi_{\text{mag}} \to \infty$, the cloud consists of abundant triplets, which lead to $M_{\text{stag}} \to \infty$.

VI. HIGHER DIMENSIONS

So far, we have discussed one-dimensional spin systems where deconfinement occurs generically in models with spin 1/2 per unit cell and confinement has to be explicitly induced by dimerization. The situation in $D \ge 2$ is quite different, as deconfinement is not generic. Instead, it has been shown that

the low-energy physics of many spin models can be written in terms of gauge-field theories. Here, the constituents are fractionalized particles (spinons) being minimally coupled to a gauge field of Z_2 or U(1) symmetry.[2,4,5] The gauge theory may have both deconfining and confining phases. While the former display true fractionalization, the gauge-field dynamics in the latter leads to confinement of objects carrying a gauge charge (e.g., spinons). The deconfined phases display topological order characterized by the suppression of topological defects of the gauge field and by nontrivial ground-state degeneracies. In contrast to 1D systems, nontrivial quantum phase transitions between confined and deconfined phases can be driven by varying microscopic model parameters.

This discussion makes clear that the physical mechanisms for deconfinement in 1D and higher dimensions are quite different. However, in both cases, a system can be in a weakly confined regime, i.e., close to deconfinement, with qualitatively similar observable consequences. In the following, we briefly sketch which of our results can be directly carried over to $D \geq 2$.

A. Confined and deconfined paramagnets

In spin models with spin 1/2 per unit cell, quantum paramagnets can come in different varieties: valence-bond solid phases spontaneously break the lattice translation symmetry and display gapped spin-1 excitations, i.e., confined spinons. In contrast, spin liquids do not break any symmetry of the Hamiltonian and feature deconfined spin-1/2 spinons, which can be gapless or gapped. In addition, spin liquids display low-lying gauge-field excitations: in the Z_2 case, these are gapped vortices of the Z_2 gauge field, dubbed "visons," whereas the U(1) case displays a linearly dispersing "photon" mode. These excitations carry zero spin, i.e., translate into singlet excitations in terms of the original spin variables.

Weak confinement can for instance be expected (i) near a paramagnetic confinement-deconfinement transition, e.g., from a VBS to a Z_2 spin liquid on the triangular lattice[46–49] and (ii) near a deconfined critical point, e.g., a transition from a VBS to a Néel state on the square lattice. In both cases, the energy scale associated to confinement will be small in the VBS phase close to the quantum critical point. Consequently, there will be a large length scale ξ_{conf}, with $\xi_{\text{conf}} \gg \xi_{\text{mag}}$, which characterizes the binding of spinons, which may be detected using nonmagnetic impurities as described above. In a VBS phase, ξ_{conf} also plays the role of a characteristic domain wall thickness.[10]

Candidates for a deconfined VBS-Néel transition are the J_1-J_2 and $J-Q$ square lattice spin-1/2 Heisenberg models, where the antiferromagnetic order is frustrated either by a second-neighbor (J_2) or ring-exchange (Q) interaction. Whereas the transition in both cases may be weakly first order, observable finite-temperature properties of the $J-Q$ model have been found to be in agreement with predictions of deconfined criticality.[50]

Indications for weak confinement have indeed been found in a numerical study[12] of the frustrated $J_1-J_2-J_3$ Heisenberg model on the square lattice, where the couplings J_i connecting i-th neighbor sites are all antiferromagnetic. For $J_3=0$, this model displays a paramagnetic phase for $0.4<J_2/J_1<0.6$, which has been proposed to be of columnar[51] or plaquette[52] VBS type. For $J_2=0$, the paramagnetic phase appears to be larger, $0.3<J_3/J_1<0.7$,[53,54] and again columnar[53] and plaquette[55,56] VBS states have been suggested. Reference 12 studied the $J_1-J_2-J_3$ model using exact diagonalization, near the line $J_2+J_3=J_1/2$ where the VBS order is likely most stable. Interestingly, these calculations showed clear indications of the existence of two length scales: while the magnetic bulk correlation length, ξ_{mag}, was rather short, a significantly larger scale could be identified in the decay of the spin polarization near a vacancy—consistent with our analysis, this is to be identified with the confinement length ξ_{conf}. For instance, for $J_{1,2,3}=(1,0.3,0.2)$, $\xi_{\text{mag}} \approx 0.7$ and $\xi_{\text{conf}} \approx 5.5$.[12] These findings (i) suggest that weak confinement is common to many frustrated low-dimensional magnets and (ii) support that the paramagnetic phase of the $J_1-J_2-J_3$ model is located near a deconfined critical point.

Among the various differences between 1D and higher dimensions is that weak confinement in $D \geq 2$ implies low-lying singlet excitations, which are energetically located below the triplet gap; in the gauge-field language, these are, e.g., visons near a confinement-deconfinement transition. In contrast, in the $J_1-J_2-\delta$ chain there are no low-lying singlets, as any excitation requires the creation of two spinons with an energy cost of at least the triplet gap.

B. Implications of linear confinement

In the language of spinons coupled to gauge fields, a treatment of the weakly confined regime is difficult, as the gauge-field effects leading to confinement are nonperturbative. In the following, we simply *assume* that the gauge field induces weak linear pairwise confinement between spinons (as well as between spinons and holons) and discuss its consequences. In fact, linear confinement is a plausible result of VBS formation in $D \geq 2$.[10] Note, however, that bound states can in principle exist in a situation of asymptotic deconfinement; see Sec. VI C.

The simplest possible analysis employs a linear confinement potential $V(\mathbf{r})=\alpha r$ in the continuum limit. Consider a confined paramagnet with a single vacancy, the latter introducing a spinon into the system. Assuming the spinon to be massive with quadratic dispersion and to be linearly bound to the vacancy, its motion is described by a D-dimensional version of Eq. (15):

$$-\frac{J}{2m}\nabla^2\Psi(\mathbf{r}) + \alpha J r \Psi(\mathbf{r}) = E\Psi(\mathbf{r}). \tag{22}$$

Here r is the radial distance from i_{imp}. The solution of the above differential equation can be written as

$$\Psi(\mathbf{r}) = \begin{cases} \psi(r)\exp(-il\theta), & D=2, \\ \psi(r)Y_l^m(\theta,\phi), & D=3, \end{cases} \tag{23}$$

where $Y_l^m(\theta,\phi)$ is a spherical harmonic.[32] Unfortunately, the resulting radial problem has no exact (analytical) solution.

We then proceed assuming that the wave function of the lowest energy vacancy-spinon bound state can be approximated by

$$\psi(r) = (r/\xi)^{\beta}\exp[-(r/\xi)^{\beta}], \tag{24}$$

where $\xi=(2m\alpha)^{-1/3}$ and the coefficient β is variationally determined. This choice is again motivated by the asymptotic form of the Airy function $\mathrm{Ai}(x)$ [see Eq. (9)]. It also satisfies the boundary conditions $\psi(0)=0$ and $\psi(\infty)=0$. By minimizing the total energy $E=\int d\mathbf{r}\Psi^{*}(\mathbf{r})H\Psi(\mathbf{r})/\int d\mathbf{r}|\Psi(\mathbf{r})|^2$, with H given by Eq. (22), it is easy to show that, for $D=2$ and $l=0$, we have

$$E = \frac{J}{2m\xi^2}\frac{\beta^2/8 + 2^{-2-3/\beta}\Gamma(2+3/\beta)}{2^{-2(1+\beta)/\beta}\Gamma(2+2/\beta)},$$

where $\Gamma(x)$ is the Gamma function.[32] The above expression assumes a minimum value $E=2.1967J/(2m\xi^2)$ for $\beta=1.1989$. Similarly, for $D=3$, one finds $E=2.5187J/(2m\xi^2)$ and $\beta=1.2682$. It is worth mentioning that the same variational procedure applied to the one-dimensional case gives $\beta=1.1428$ and $E=2.4429J/(2m\xi^2)$, which is a good approximation for the exact analytical solution of Eq. (22), $E=2.3381J/(2m\xi^2)$, calculated in Ref. 20.

We conclude that the vacancy physics in the weakly confined regime in $D\geq 2$ is also dominated by the confinement length: Eq. (24) has a maximum for $r=\xi$, which can be identify with ξ_{conf}. As we move deep into the weakly confined region (smaller α), ξ increases. The spin polarization cloud around i_{imp}, whose characteristic length scale is $\xi=\xi_{\mathrm{conf}}$, does not display a pure exponential decay, but instead has a profile similar to the 1D case. This also suggests that analyzing the numerical data in terms of an exponential decay, as done in Ref. 12, might be not appropriate in the weakly confined regime.

Two-spinon bound states can be addressed similarly. The starting point is the D-dimensional version of Eq. (10) from Ref. 35, which is nothing but Eq. (22) with the replacements: $m\rightarrow\mu=m/2$ and $E\rightarrow E-\Delta$. Here μ is the reduced mass, Δ is the spin gap (the energy of the lowest bound state), and r is the relative radial distance between the two spinons. As a consequence, the characteristic length scale is now $\xi=(2\mu\alpha)^{-1/3}$. The solutions of the effective Schrödinger equation, which describes the two-spinon bound states *above* the spin-gap Δ, also have form (23). We assume that Eq. (24) is a good approximation for the radial part of the first bound-state wave function $\psi_1(r)$ and variationally determine the parameter β and the energy E_1 for the case $l=0$. Once β is known, variational wave functions for higher bound states can be easily constructed just by multiplying $\psi_1(r)$ by a polynomial, e.g.,

$$\psi_2(r) = [(r/\xi)^2 + c_{21}]\psi_1(r),$$

$$\psi_3(r) = [(r/\xi)^4 + c_{32}(r/\xi)^2 + c_{31}]\psi_1(r), \tag{25}$$

respectively, for the second and third lowest-energy bound state above Δ. The coefficients c_{ij} are determined by requiring that the states are orthogonal to each other. Notice that Eq. (25) satisfy the boundary condition $\psi(0)=0$ and they vanish for large r. The *ansatz* (25) follows from a careful analysis of the analytical solutions of the one-dimensional problem. Indeed, we applied the above procedure for the $D=1$ case, compared the results with the analytical solution reported in Ref. 35, and verified that it provides good estimates for the energy of the lowest two-spinon bound states.

For $D=2$ and $l=0$, we find again $\beta=1.1989$ and that the energies of the first (E_1), second (E_2), and third (E_3) lowest bound states are given by $E_i=e_i+\Delta$ with $e_1=2.1967$, $e_2=4.0025$, and $e_3=5.4875J/(2\mu\xi^2)$. According to the discussion in Sec. V A, the strong-weak confinement crossover occurs when $e_1\sim\Delta$. Similar considerations hold for $D=3$.

The above analysis suggests many parallels between 1D and higher dimensions, but falls short of capturing short-distance features of the bound states as well as effects of nontrivial statistics of the spinons.

C. Asymptotic confinement vs short-range bound states

The preceding discussion of confinement has been simplistic in that it assumed that the presence or absence of long-distance (asymptotic) confinement also determines the nature of the low-energy excitations. While this is the case for the one-dimensional $J_1-J_2-\delta$ spin chain, which features a confinement potential of the type $V(x)=\alpha|x|$ for all length scales, this is obviously not true in general. While the long-distance behavior of the effective interaction, mediated by the gauge field, decides about asymptotic confinement or deconfinement, it is its short-distance behavior which determines the existence and spatial size of possible bound states at low energies.

In other words, it is conceivable that a phase in $D\geq 2$ spatial dimensions with asymptotic deconfinement of spinons and associated topological order displays short-distance spinon bound states.[57] In such a situation, the diagnostics proposed in this paper, i.e., a vacancy-induced magnetic moment with cloud size ξ_{conf} and multiple sharp modes in χ'' below the continuum, will signal (weak) confinement, whereas the true nature of the phase is deconfined. Obviously, distinguishing such a deconfined phase with bound states from a confined phase is extremely difficult. (Numerically, topological ground-state degeneracies may be used to detect deconfinement.)

To our knowledge, no explicit microscopic examples for fractionalized spin liquids with spinon bound states existing below the continuum are known to date,[58] which is also related to the difficulties in numerically studying the excitation spectra of the relevant microscopic models. Possible candidates are states with Z_2 fractionalization which are believed to generically display a nonzero spinon pairing amplitude.[59] It should be kept in mind that the bound states in question, which are determined by short-range physics, are not necessarily part of effective low-energy gauge-field descriptions. It is worth noting that a spinless impurity in the VBS phase near a deconfined critical point has been shown[60] to bind a spinon on a length scale much shorter than the VBS (or confinement) length.

VII. SUMMARY

In this paper, we have argued that quantum paramagnets, in particular those with frustration, can display an interesting

regime of weak confinement of spinons. Here, the long-distance properties are conventional, with elementary excitations being spin-1 triplons; however, the physics of spinons is visible at shorter length scales. Such weakly confined paramagnets are characterized by two potentially large length scales, namely, the common magnetic correlation length ξ_{mag} and a confinement length ξ_{conf}, which measures the typical distance between weakly bound spinons. Weak confinement implies $\xi_{\mathrm{conf}} \gg \xi_{\mathrm{mag}}$; the crossover to strong confinement occurs at $\xi_{\mathrm{conf}} \approx \xi_{\mathrm{mag}}$.

We have illustrated the physics of the weakly confined regime with explicit calculations for frustrated dimerized spin chains, where weak confinement can be realized for weak explicit dimerization on top of strong spontaneous dimerization. In particular, we have studied the static response of the system to nonmagnetic impurities: the staggered polarization cloud induced by the impurity decays on a length scale given by $\max(\xi_{\mathrm{conf}}, \xi_{\mathrm{mag}})$. We have also briefly discussed the structure of the dynamic susceptibility in the clean case and the effective interaction between impurity-induced moments. Qualitatively, our results remain valid in higher dimensions as well: in $D \geq 2$, weak confinement is reached near a confinement-deconfinement transition, e.g., between a gapped spin liquid and a valence-bond solid, or near a deconfined quantum critical point between a Néel and a VBS phase.

However, a caveat in $D \geq 2$ is that long-distance confinement (deconfinement) of spinons is not necessarily equivalent to the presence (absence) of short-distance spinon bound states: in principle, bound states forming conventional triplon excitations can exist even in deconfined spin liquids. This tantalizing scenario is left for future investigations.

Last not least, upon inclusion of mobile charge carriers, weak confinement can be expected to lead to an almost spin-charge separated metallic state. This may be a conventional Fermi liquid but with small quasiparticle weights and strong incoherent continua in spectral functions: the carriers will get dressed by a large cloud of *singlet* excitations, in analogy to the dressing with *triplet* excitations near a magnetic quantum critical point.[61]

ACKNOWLEDGMENTS

We thank R. Moessner, A. Rosch, S. Sachdev, U. Schollwöck, T. Senthil, and G. Japaridze for discussions and S. Trebst for suggestions. This research was supported by the DFG through SFB 608 (Köln).

APPENDIX: VARIATIONAL APPROACH FOR THE DISORDER LINE

In this section we present some details of the variational calculations discussed in Sec. IV A. We start by looking at the overlap between the states $|m\rangle$ and $|p\rangle$. By comparing the two states one can see that there is a mismatch in the position of the singlets in the region between the sites $2m$ and $2p$. Each mismatch contributes with a factor $(-1/2)$ and the number of mismatches is equal to $|m-n|$. Thus, Eq. (4) follows.

In order to calculate the matrix elements (5) it is convenient to introduce the operator[17]

$$h(i,j) = \frac{1}{2}(1 - 4\mathbf{S}_i \cdot \mathbf{S}_j). \tag{A1}$$

By applying the operator $h(i,j)$ to a normalized singlet combination $[i,j]$ or a product of them, we have

$$h(i,j)[i,j] = 2[i,j],$$

$$h(i,j)[k,i][j,l] = (-1)[k,l][i,j],$$

$$h(i,j)[k,i][l,j] = [k,j][i,l] + [k,i][l,j]. \tag{A2}$$

In the presence of an unpaired spin $|\uparrow\rangle_i$ the following expressions hold:

$$h(i,j)[l,i]|\uparrow\rangle_j = (-1)|\uparrow\rangle_l[i,j],$$

$$h(i,j)|\uparrow\rangle_i[j,l] = (-1)[i,j]|\uparrow\rangle_l,$$

$$h(i,j)[i,l]|\uparrow\rangle_j = |\uparrow\rangle_i[l,j] + [i,l]|\uparrow\rangle_j. \tag{A3}$$

Instead of the Hamiltonian (1) with a nonmagnetic impurity at $i_{\mathrm{imp}}=1$, we consider an auxiliary one H', which is defined as

$$H' = -2H + (J_1 + J_2)(N-1). \tag{A4}$$

The above equation can be written in terms of the operator $h(i,j)$ [Eq. (A1)], namely, $(J_1=1)$,

$$H' = (1+\delta)\sum_{i=2}^{N} h(2i-1,2i) + (1-\delta)\sum_{i=1}^{N-1} h(2i,2i+1) + J_2\sum_{i=2}^{N-1} h(2i-1,2i+1) + J_2\sum_{i=1}^{N} h(2i,2i+2). \tag{A5}$$

Using properties (A2) and (A3) we can calculate $H'|p\rangle$. For instance, the contribution of the first term of Eq. (A5) reads

$$\sum_{i=2}^{N} h(2i-1,2i)|p\rangle = 2(N-p)|p\rangle - |p-1\rangle - \sum_{i=2}^{p-1} |i,p\rangle.$$

The state $|i,p\rangle$ is quite similar to $|p\rangle$ apart from the fact that a long singlet is introduced in the vicinity of the site $2i$, i.e.,

$$|i,p\rangle = [1,2][3,4]\ldots[2i-1,2i][2i-2,2i+1]\ldots|\uparrow\rangle_{2p}\ldots \times[2N-3,2N-2][2N-1,2N].$$

For the second term of Eq. (A5) we have

$$\sum_{i=1}^{N-1} h(2i,2i+1)|p\rangle = 2(p-1)|p\rangle - |p+1\rangle - \sum_{i=p+1}^{N-1} |i,p\rangle',$$

with

$$|i,p\rangle' = [1,2][3,4]\ldots|\uparrow\rangle_{2p}\ldots[2i,2i+1] \times[2i-1,2i+2]\ldots[2N-1,2N].$$

Notice that $|i,p\rangle$ and $|i,p\rangle'$ are similar, but for the former we have $i<p$ while for the latter, $i>p$. The results for the two

remaining terms can also be expressed in terms of $|p\rangle$, $|p\pm 1\rangle$, $|i,p\rangle$, and $|i,p\rangle'$. With the help of Eq. (A4) it is possible to show that

$$\begin{aligned}2(H-\bar{E}_0)|p\rangle &= (4p\delta+1+3J_2-2\delta)|p\rangle - J_2|\chi_p\rangle \\ &+ (1+\delta-J_2)|p-1\rangle + (1-\delta-J_2)|p+1\rangle \\ &+ (1+\delta-2J_2)\sum_{i=1}^{p-1}|i,p\rangle \\ &+ (1-\delta-2J_2)\sum_{i=p+1}^{N-1}|i,p\rangle', \end{aligned} \tag{A6}$$

where $\bar{E}_0=-(1/4)(1+2\delta+J_2)(2N)$ and the state $|\chi_p\rangle$ is given by

$$|\chi_p\rangle = (-1)[1,2][3,4]\ldots[2p-2,2p+2][2p-1,2p+1]$$

$$|\uparrow\rangle_{2p}\ldots[2N-3,2N-2][2N-1,2N].$$

Proceeding in the same way as for Eq. (4), one can show that the overlaps between $|m\rangle$ and the states $|\chi_p\rangle$, $|i,p\rangle$, and $|i,p\rangle'$ are given by

$$\langle m|\chi_p\rangle = (1/2)\langle m|p\rangle,$$

$$\begin{aligned}\langle m|i,p\rangle &= -\frac{1}{2}\langle m|p\rangle\{\theta(m-p)+\theta(p-m-1) \\ &\times[\theta(m-i)+4\theta(i-m-1)]\}, \end{aligned}$$

$$\begin{aligned}\langle m|i,p\rangle' &= -\frac{1}{2}\langle m|p\rangle\{\theta(p-m)+\theta(m-p-1) \\ &\times[\theta(i-m)+4\theta(m-i-1)]\}, \end{aligned} \tag{A7}$$

where the function $\theta(x)$ is defined as

$$\theta(x)=\begin{cases}1, & x\geq 0\\ 0, & x<0.\end{cases} \tag{A8}$$

Equation (5) follows from Eqs. (A6) and (A7).

[1] T. Giamarchi, *Quantum Physics in One Dimension* (Clarendon Press, Oxford, 2003).
[2] P. A. Lee, N. Nagaosa, and X.-G. Wen, Rev. Mod. Phys. **78**, 17 (2006).
[3] *Composite Fermions*, edited by O. Heinonen (World Scientific, Singapore, 1998).
[4] S. Sachdev, in *Quantum Magnetism*, Lecture Notes in Physics Vol. 645, edited by U. Schollwöck, J. Richter, D. J. J. Farnell, and R. A. Bishop (Springer, Berlin, 2004).
[5] S. Sachdev, Nat. Phys. **4**, 173 (2008).
[6] R. Moessner and S. L. Sondhi, Phys. Rev. Lett. **86**, 1881 (2001).
[7] A. Kitaev, Ann. Phys. (N.Y.) **303**, 2 (2003).
[8] A. Kitaev, Ann. Phys. (N.Y.) **321**, 2 (2006).
[9] G. Misguich, C. Lhuillier, B. Bernu, and C. Waldtmann, Phys. Rev. B **60**, 1064 (1999).
[10] T. Senthil, L. Balents, S. Sachdev, A. Vishwanath, and M. P. A. Fisher, Phys. Rev. B **70**, 144407 (2004).
[11] A. W. Sandvik, Phys. Rev. Lett. **98**, 227202 (2007).
[12] D. Poilblanc, A. Läuchli, M. Mambrini, and F. Mila, Phys. Rev. B **73**, 100403(R) (2006); D. Poilblanc, M. Mambrini, A. Läuchli, and F. Mila, J. Phys.: Condens. Matter **19**, 145205 (2007).
[13] R. Chitra, S. Pati, H. R. Krishnamurthy, D. Sen, and S. Ramasesha, Phys. Rev. B **52**, 6581 (1995).
[14] S. Pati, R. Chitra, D. Sen, S. Ramasesha, and H. R. Krishnamurthy, J. Phys.: Condens. Matter **9**, 219 (1997).
[15] K. Okamoto and K. Nomura, Phys. Lett. A **169**, 433 (1992).
[16] I. Affleck, in *Dynamical Properties of Unconventional Magnetic Systems*, NATO Advanced Study Institute, Series E: Applied Sciences, edited by A. Skjeltrop and D. Sherrington (Kluwer Academic, Dordrecht, 1998), Vol. 349, pp. 123-131; See also arXiv:cond-mat/9705127v1.
[17] C. K. Majumdar and D. K. Ghosh, J. Math. Phys. **10**, 1388 (1969).
[18] B. S. Shastry and B. Sutherland, Phys. Rev. Lett. **47**, 964 (1981).
[19] E. Sørensen, I. Affleck, D. Augier, and D. Poilblanc, Phys. Rev. B **58**, R14701 (1998).
[20] G. S. Uhrig, F. S. Schönfeld, M. Laukamp, and E. Dagotto, Eur. Phys. J. B **7**, 67 (1999).
[21] Two-spinon bound states can be of $S=0$ or $S=1$ character. The lowest $S=1$ two-spinon bound state is the conventional triplon excitation. (For the spin chain, the lowest $S=0$ bound state is the ground state itself.) In the limit of weak confinement, the energetic difference between singlet and triplet spinon bound states becomes small for higher excited states, as the magnetic interaction between two distant spinons is small.
[22] S. R. White, Phys. Rev. B **48**, 10345 (1993); U. Schollwöck, Rev. Mod. Phys. **77**, 259 (2005).
[23] F. Alet *et al.* (ALPS collaboration), J. Phys. Soc. Jpn. Suppl. **74**, 30 (2005); F. Albuquerque *et al.* (ALPS collaboration), J. Magn. Magn. Mater. **310**, 1187 (2007); see http://alps.comp-phys.org
[24] M. Sigrist and A. Furusaki, J. Phys. Soc. Jpn. **65**, 2385 (1996).
[25] S. Sachdev and M. Vojta, *Proceedings of the XIII International Congress on Mathematical Physics, London*, edited by A. Fokas *et al.* (International Press, Boston, 2001).
[26] B. Normand and F. Mila, Phys. Rev. B **65**, 104411 (2002).
[27] T. Miyazaki, M. Troyer, M. Ogata, K. Ueda, and D. Yoshioka, J. Phys. Soc. Jpn. **66**, 2580 (1997).
[28] G. B. Martins, M. Laukamp, J. Riera, and E. Dagotto, Phys. Rev. Lett. **78**, 3563 (1997); M. Laukamp, G. B. Martins, C. Gazza, A. L. Malvezzi, E. Dagotto, P. M. Hansen, A. C. Lopez, and J. Riera, Phys. Rev. B **57**, 10755 (1998).
[29] C. Yasuda, S. Todo, M. Matsumoto, and H. Takayama, Phys. Rev. B **64**, 092405 (2001) and references therein.
[30] M. Vojta, C. Buragohain, and S. Sachdev, Phys. Rev. B **61**, 15152 (2000).
[31] S. Sachdev and M. Vojta, Phys. Rev. B **68**, 064419 (2003).
[32] M. Abramowitz and I. A. Stegun, *Handbook of Mathematical*

Functions (Dover Publications, New York, 1964).
[33] H. Fukuyama, T. Tanimoto, and M. Saito, J. Phys. Soc. Jpn. **65**, 1182 (1996).
[34] N. Laflorencie and D. Poilblanc, Phys. Rev. Lett. **90**, 157202 (2003).
[35] T. M. R. Byrnes, M. T. Murphy, and O. P. Sushkov, Phys. Rev. B **60**, 4057 (1999).
[36] S. Trebst, H. Monien, C. J. Hamer, Z. Weihong, and R. R. P. Singh, Phys. Rev. Lett. **85**, 4373 (2000).
[37] W. Zheng, C. J. Hamer, R. R. P. Singh, S. Trebst, and H. Monien, Phys. Rev. B **63**, 144411 (2001).
[38] K. P. Schmidt, C. Knetter, and G. S. Uhrig, Phys. Rev. B **69**, 104417 (2004).
[39] M. Takigawa, N. Motoyama, H. Eisaki, and S. Uchida, Phys. Rev. B **55**, 14129 (1997).
[40] F. Tedoldi, R. Santachiara, and M. Horvatic, Phys. Rev. Lett. **83**, 412 (1999).
[41] M. Hase, K. Uchinokura, R. J. Birgeneau, K. Hirota, and G. Shirane, J. Phys. Soc. Jpn. **65**, 1392 (1996).
[42] M. C. Martin, M. Hase, K. Hirota, G. Shirane, Y. Sasago, N. Koide, and K. Uchinokura, Phys. Rev. B **56**, 3173 (1997).
[43] L. P. Regnault, J. P. Renard, G. Dhalenne, and A. Revcolevschi, Europhys. Lett. **32**, 579 (1995).
[44] M. Azuma, Y. Fujishiro, M. Takano, M. Nohara, and H. Takagi, Phys. Rev. B **55**, R8658 (1997).
[45] A. Oosawa, T. Ono, and H. Tanaka, Phys. Rev. B **66**, 020405(R) (2002).
[46] S. Sachdev and N. Read, Int. J. Mod. Phys. B **5**, 219 (1991).
[47] C. Xu and S. Sachdev, Phys. Rev. B **79**, 064405 (2009).
[48] R. A. Jalabert and S. Sachdev, Phys. Rev. B **44**, 686 (1991); S. Sachdev and M. Vojta, J. Phys. Soc. Jpn. **69**, Suppl. B, 1 (2000).
[49] R. Moessner and S. L. Sondhi, Phys. Rev. B **63**, 224401 (2001).
[50] R. G. Melko and R. K. Kaul, Phys. Rev. Lett. **100**, 017203 (2008).
[51] N. Read and S. Sachdev, Phys. Rev. Lett. **62**, 1694 (1989).
[52] M. E. Zhitomirsky and K. Ueda, Phys. Rev. B **54**, 9007 (1996).
[53] P. W. Leung and Ngar-wing Lam, Phys. Rev. B **53**, 2213 (1996).
[54] L. Capriotti, D. J. Scalapino, and S. R. White, Phys. Rev. Lett. **93**, 177004 (2004).
[55] M. Mambrini, A. Läuchli, D. Poilblanc, and F. Mila, Phys. Rev. B **74**, 144422 (2006).
[56] M. Arlego and W. Brenig, Phys. Rev. B **78**, 224415 (2008).
[57] The existence of short-distance bound states in the presence of long-distance deconfinement is well known in quantum electrodynamics: the $(-1/r)$ Coulomb potential of two opposite charges allows for both scattering and bound states (e.g., the hydrogen atom).
[58] An exception appears to be the toric code model in a transverse field, where bound states have been seen in the topologically ordered phase: J. Vidal, R. Thomale, K. P. Schmidt, and S. Dusuel, arXiv:0902.3547 (unpublished).
[59] T. Senthil and M. P. A. Fisher, Phys. Rev. B **62**, 7850 (2000); **63**, 134521 (2001).
[60] A. Kolezhuk, S. Sachdev, R. R. Biswas, and P. Chen, Phys. Rev. B **74**, 165114 (2006).
[61] S. Sachdev, M. Troyer, and M. Vojta, Phys. Rev. Lett. **86**, 2617 (2001).